



## Self-supported crystalline-amorphous composites of metal phosphate and NiS for high-performance water electrolysis under industrial conditions

Lei Guo <sup>a,b,c</sup>, Jing Xie <sup>a,b,c</sup>, Shiyi Chen <sup>a,b,c</sup>, Zexing He <sup>a,b,c</sup>, Yuezheng Liu <sup>a,b,c</sup>, Chengxiang Shi <sup>a,b,c</sup>, Ruijie Gao <sup>a,b,c</sup>, Lun Pan <sup>a,b,c</sup>, Zhen-Feng Huang <sup>a,b,c,\*</sup>, Xiangwen Zhang <sup>a,b,c</sup>, Ji-Jun Zou <sup>a,b,c,\*</sup>

<sup>a</sup> Key Laboratory for Green Chemical Technology of the Ministry of Education, Institute of Molecular Plus, School of Chemical Engineering and Technology, Tianjin University, Tianjin 300072, China

<sup>b</sup> Collaborative Innovative Center of Chemical Science and Engineering (Tianjin), Tianjin 300072, China

<sup>c</sup> Zhejiang Institute of Tianjin University, Ningbo, Zhejiang 315201, China



### ARTICLE INFO

#### Keywords:

Water electrolysis  
Self-supported integrated electrode  
Crystalline-amorphous composites  
Large current density  
AEMWE

### ABSTRACT

Developing affordable and efficient electrocatalysts toward water electrolysis under industrial conditions is crucial for large-scale production of green hydrogen. In this regard, we propose a facile and mild method to construct crystalline-amorphous composites of metal phosphate (MPi) and NiS on nickel foam (NF) for practical water electrolysis. The as-prepared electrodes exhibit excellent performance, achieving a remarkable current density of 1000 mA cm<sup>-2</sup> at the ultralow overpotential of 345 and 223 mV for FePi-NiS/NF (oxygen evolution reaction, OER) and NiCoPi-NiS/NF (hydrogen evolution reaction, HER), respectively. The composites can undergo an in-situ transformation into highly active and targeted species under high current density, which possess a unique pore structure interconnected by nanosheets that provides an abundance of catalytic sites and open channels for efficient bubble diffusion. When operated under industrial conditions (6 M KOH, 70 °C), the assembled electrode requires only 1.712 V to attain a current density of 1000 mA cm<sup>-2</sup>. The electrodes also demonstrate exceptional performance in alkaline electrolysis with an anion exchange membrane (AEMWE) when scaled up to a larger size (area:  $\approx 25 \text{ cm}^2$ ). Specifically, they achieve a substantial current of 12.5 A at 1.87 V with a high energy efficiency of 79.2 % and remarkable durability over 30 h under industrial electrolysis conditions (1 M KOH, 50 °C), outperforming benchmark Pt/C/NF || IrO<sub>2</sub>/NF electrodes with energy saving of 0.215 kWh Nm<sup>-3</sup>. This work provides a cost-effective and efficient strategy for designing and constructing stable and active catalysts for water electrolysis under harsh industrial conditions.

### 1. Introduction

Building a clean and renewable energy system is crucial for promoting the sustainable development of society [1]. Hydrogen, as a sustainable and clean energy source with zero carbon emissions and ultra-high energy density (120–142 MJ kg<sup>-1</sup>), is envisioned as a potential substitute for fossil fuels [2,3]. Electrochemical water splitting is one of the most environmental-friendly and cost-effective hydrogen production technologies [4]. At present, Pt-based and Ir/Ru-based catalysts are still recognized as benchmark electrocatalysts for the hydrogen evolution reaction (HER) and the oxygen evolution reaction (OER), respectively. However, the scarcity and high cost of noble-metal

materials severely limit the widespread implementation of water electrolysis. Therefore, there is an urgent need to develop low-cost and earth-abundant electrocatalysts with exceptional performance to advance the industrialization of hydrogen production through water electrolysis.

In recent years, researchers have developed numerous electrocatalysts, including transition metal based oxides, hydroxides, carbides, nitrides, phosphides, sulfides, selenide, etc. [5–7]. Among these, sulfides have been developed as efficient bifunctional electrocatalysts for water splitting due to their high conductivity, mild synthesis conditions, and abundant natural reserves. Studies have shown that the active sites of metal sulfides resemble hydrogenase, enabling the transformation of

\* Corresponding authors at: Key Laboratory for Green Chemical Technology of the Ministry of Education, Institute of Molecular Plus, School of Chemical Engineering and Technology, Tianjin University, Tianjin 300072, China.

E-mail addresses: [zhuang@tju.edu.cn](mailto:zhuang@tju.edu.cn) (Z.-F. Huang), [jj\\_zou@tju.edu.cn](mailto:jj_zou@tju.edu.cn) (J.-J. Zou).

protons and electrons into molecular hydrogen at low potentials [8]. Meanwhile, the hydroxyl oxide species in-situ formed by the reconstruction of sulfides during OER process exhibit high activity [9–11]. Although monometallic sulfide exhibits significant performance in water electrolysis, the performance at high current density still not satisfactory. To meet the industrial demand of activity and stability under practical conditions, the key problems that need to be solved urgently are as follows: (1) More abundant active sites are often required under industrial current density; (2) The intrinsic activity of metal sulfide needs to be improved, due to the unoptimized electronic structure of sulfides. Researchers have attempted numerous strategies to address the aforementioned issues, such as doping, defect engineering, morphology engineering, etc. [12]. Among them, composite catalysts not only introduce multiple active sites but also improve the electronic structure of active sites through charge redistribution, thereby enhancing their intrinsic activity [13]. In addition, phosphates have also been widely studied as catalysts for water electrolysis. Studies have shown that phosphate groups can be used as effective proton carriers to accelerate proton transfer, and their flexible coordination helps to stabilize the intermediate state, thereby improving the performance of OER [14]. Theoretical calculations also showed that phosphate has a low energy barrier for the adsorption of hydrogen atoms which can be used as an efficient HER catalyst [15]. However, the performance of these catalysts at industrial current densities needs to be further investigated to evaluate their industrial application potential.

Compared with crystalline materials, amorphous materials offer several advantages [16–18]: (1) the presence of sufficient unsaturated coordination sites and dangling bonds with random orientation enhances the adsorption of reactants, thus providing more active sites; (2) the highly defective structure and disordered atomic arrangement facilitate ion diffusion and electron transfer, accelerating reaction kinetics; (3) the flexible and metastable structure of amorphous materials triggers self-reconstruction during electrocatalytic process, enabling good reaction adaptability. However, the amorphous phase still exhibits inherent drawbacks such as high cation dissolution rates, poor conductivity, and low stability [19]. So, constructing a crystalline-amorphous composite is an effective strategy for fabricating highly active and stable catalysts.

Combining the advantages of alkaline water electrolysis (AWE) and proton-exchange membrane water electrolysis (PEMWE), anion-exchange membrane water electrolysis (AEMWE) has emerged as a promising technology for water electrolysis. However, AEMWE technology is still in its early stage, and its performance at a large scale is yet to be explored to facilitate industrialization. In addition, for powder catalysts, the preparation of membrane electrode assemblies (MEA) often involves spraying or decal transfer methods, which not only increases process complexity but also presents challenges such as low catalyst utilization and blocked mass transfer [20]. By employing self-supported integrated electrodes, the integration of catalyst layers (CL) and porous transport layers (PTL) not only improves the mechanical stability of MEA, but also facilitates the emission of gas products [21,22]. Therefore, applying self-supported electrodes in AEMWE holds the potential to further enhance system performance, enabling high-efficiency hydrogen production with low energy consumption under harsh industrial conditions. To advance the industrialization process, there is an urgent need to develop a rapid and large-scale electrode production method under mild conditions. Currently, methods such as electrochemical deposition, water/solvothermal synthesis, wet chemical methods, vapor deposition, and more are used to prepare self-supported electrodes [23]. Among these, electrodeposition method and wet chemical method are relatively fast and mild strategies for catalysts preparation.

Herein, we propose a mild and universal method to prepare crystalline-amorphous integrated composites of MPi-NiS (M=Fe, Co, Ni) for high-performance industrial water electrolysis. This stable integrated structure and the interaction between composites synergistically

improve the catalyst performance at high current densities. Notably, the crystalline-amorphous structure leads to partial reconstruction of the catalysts during the reaction process. Specifically, the in-situ generated NiOOH/FeOOH with abundant oxygen vacancies reconstructed from FePi-NiS/NF exhibit high OER activity, enabling a high current density of  $1000 \text{ mA cm}^{-2}$  to be achieved with only 345 mV in 1 M KOH electrolyte. Similarly, the in-situ formed Co(OH)<sub>2</sub>/Ni(OH)<sub>2</sub> derived from NiCoPi-NiS/NF promote the HER dynamics, requiring an ultralow overpotential of 223 mV to deliver  $-1000 \text{ mA cm}^{-2}$ . Moreover, the reconstructed species exhibit nanosheets structures with rich pores, facilitating the exposure of active sites and bubble diffusion. Furthermore, scaled-up NiCoPi-NiS/NF || FePi-NiS/NF electrodes demonstrate outstanding performance in AEMWE, enabling an ultrahigh current of 12.5 A to be achieved at 1.87 V, which represents a significant energy saving of 0.215 kWh/Nm<sup>3</sup> H<sub>2</sub> compared to commercial electrodes. Additionally, our catalysts were operated stably over a period of 30 h under industrial conditions (12.5 A, 50 °C). This work provides a general method for developing economical and practical electrocatalysts for large-scale green hydrogen production.

## 2. Experimental section

### 2.1. Chemicals and materials

Sodium hypophosphite (NaH<sub>2</sub>PO<sub>2</sub>, 99 %), sodium sulfide nonahydrate (Na<sub>2</sub>S·9 H<sub>2</sub>O, 99 %), ferric chloride hexahydrate (FeCl<sub>3</sub>·6 H<sub>2</sub>O, 99.9 %) nickel chloride hexahydrate (NiCl<sub>2</sub>·6 H<sub>2</sub>O, 99.9 %), anhydrous cobalt chloride (CoCl<sub>2</sub>, 99.5 %) and sodium acetate (NaOAc, 99.9 %) were purchased from MACKLIN (Shanghai, China). Potassium hydroxide (KOH, 99.999 %) and sodium chloride (NaCl, 99.5 %) were purchased from Aladdin Ltd. (Shanghai, China). Hydrochloric acid (HCl, AR) was obtained from Fengchuan Chemical Reagent Co.,Ltd (Tianjin, China). Ethanol (C<sub>2</sub>H<sub>5</sub>OH, 99.9 %) was obtained from Jiangtian Chemical Co.,Ltd. (Tianjin, China). Commercial platinum carbon powder (Pt/C, 20 wt%) was purchased from Johnson Matthey Chemicals Ltd (Shanghai, China). Iridium oxide powder (IrO<sub>2</sub>) were purchased from Strem Chemicals, Inc (Shanghai, China). Graphite carbon (Vulcan XC-72R) was purchased from Sigma-Aldrich. Nafion solution (5 wt%) was purchased from Tianjin Incole Union Technology Co.,Ltd. Nickel foam with a thickness of 1.6 mm was purchased from Kunshan Jiayisheng Co., Ltd. (Jiangsu, China). All the chemicals were used directly as received without any further purification. Ultrapure water (Millipore,  $> 18.2 \text{ M}\Omega \cdot \text{cm}$ ) was used throughout the experiments.

### 2.2. Preparation of NiS/NF

Firstly, NF (1 cm × 3 cm × 0.16 cm) was cleaned by ultrasonic in HCl (3 M), ethanol and deionized water for 15 min, respectively. Then, the treated NF was put into the prepared 50 mL 0.5 M Na<sub>2</sub>S solution, and the NiS/NF precursor can be obtained after stirring the solution for 4 h at 50 °C. Finally, NiS/NF was cleaned by deionized water and ethanol, followed by drying in oven at 60 °C.

### 2.3. Preparation of NiCoPi-NiS/NF and FePi-NiS/NF

NiCoPi-NiS/NF and FePi-NiS/NF integrated electrodes with a mass loading of  $\sim 8 \text{ mg cm}^{-2}$  were prepared by constant voltage deposition using NiS/NF precursor as working electrode, graphite rod as counter electrode and Ag/AgCl as reference electrode. Specifically, the electrodeposition solution (100 mL) of NiCoPi-NiS/NF containing of NiCl<sub>2</sub>·6 H<sub>2</sub>O (1.7828 g), CoCl<sub>2</sub> (0.3246 g), NaH<sub>2</sub>PO<sub>2</sub>·H<sub>2</sub>O (2.65 g), NaCl (1.46 g), and NaOAc (0.8203 g), with a deposition voltage of  $-1.6 \text{ V}$ ; The electrodeposition solution (100 mL) of FePi-NiS/NF containing FeCl<sub>3</sub> (0.2704 g), NaH<sub>2</sub>PO<sub>2</sub>·H<sub>2</sub>O (2.65 g), NaCl (1.46 g), and NaOAc (0.8203 g), with a deposition voltage of  $-1.4 \text{ V}$ . The duration of electrodeposition is all 300 s. As comparison, NiCoPi/NF and FePi/NF samples were

synthesized on NF by the same electrodeposition steps.

#### 2.4. Preparation of $5 \times 5 \text{ cm}^2$ NiCoPi-NiS/NF and FePi-NiS/NF

The NF ( $5 \times 5 \text{ cm}^2$ ) was first pre-treated according to Section 2.2. It was then placed in a 1 M  $\text{Na}_2\text{S}$  solution, stirred at 50 °C for 12 h and subsequently washed and dried to obtain the amplified NiS/NF precursor. The NiS/NF precursor was utilized as the working electrode, while carbon paper ( $5 \times 5 \text{ cm}^2$ ) and Ag/AgCl electrode were selected as reference electrode and counter electrode, respectively. The concentration of the electrodeposition solution was increased 25 times, with a deposition current of  $-1.5 \text{ A}$  and a deposition time of 30 min on each side of the precursor.

#### 2.5. Preparation of Pt/C/NF and $\text{IrO}_2/\text{NF}$

Initially, 1 mg carbon black, 200  $\mu\text{L}$   $\text{H}_2\text{O}$ , 770  $\mu\text{L}$  ethanol and 30  $\mu\text{L}$  Nafion solution were mixed together with either 5 mg Pt/C or  $\text{IrO}_2$  in a 1 mL ink and evenly dispersed using ultrasonic technology. Subsequently, the prepared ink was slowly and evenly dripped onto the treated NF for several times until the loading mass reaches  $3 \text{ mg cm}^{-2}$ . Lastly, the obtained products Pt/C/NF and  $\text{IrO}_2/\text{NF}$  were left to dry naturally.

#### 2.6. Characterization

X-ray diffraction (XRD) patterns were acquired on MiniFlex600 X-ray diffractometer with  $\text{Cu K}\alpha$  radiation ( $\lambda = 1.54 \text{ \AA}$ ) at 40 kV and 40 mA ( $5^\circ \text{ min}^{-1}$  from 10° to 90°). The surface morphology images were obtained by Apreo S LoVac field-emission scanning electron microscope (FESEM, FEI, Czech). Lattice fringe information and energy dispersive spectrum (EDX) were recorded via a JEM-F200 transmission electron microscope operated at 200 kV. X-ray photoelectron spectrum (XPS) measurements were performed on a K-Alpha+ instrument using  $\text{Al K}\alpha$  radiation source. Quasi in-situ Raman spectra was recorded by Raman spectrometer (DXR Microscope) using a green semiconductor laser (532 nm). Specifically, Raman testing will be conducted after applying different potential to HER and OER catalysts for 1 h ( $-0.1$  to  $-0.4 \text{ V}$  for HER and  $1.3$ – $1.6 \text{ V}$  for OER).

#### 2.7. Electrochemical Measurements

Electrochemical tests were performed on an Ivium-164 workstation (IVIUMSTAT, the Netherlands) with a standard three-electrode or two-electrode configuration. The as-prepared catalysts were directly used as working electrode, and the graphite rod and a  $\text{Hg}/\text{HgO}$  electrode were used as the counter and reference electrode, respectively. The overall water splitting performance was tested in a two-electrode system with voltage ranges from 1.1 to 2.5 V at different temperature. The stability of the catalysts in two-electrode system is tested by chronoamperometry. The impregnation area of working electrodes was  $0.5 \text{ cm}^2$ . The potentials were referenced to the reversible hydrogen electrode (RHE) through following equation:

$$E_{\text{RHE}} = E_{\text{Hg/HgO}} + 0.922 \text{ V} \quad (1)$$

Linear sweep voltammetry (LSV) curves were collected with the scan rate of  $2 \text{ mV s}^{-1}$ . LSV and Tafel curves were corrected by 95 % iR compensation for the ohmic loss except for AEMWE test. Electrochemical impedance spectroscopy (EIS) was recorded in the frequency ranges from 100k Hz to 0.1 Hz and the amplitude of 10 mV at  $-0.1 \text{ V}$  (HER) and  $1.5 \text{ V}$  (OER) vs. RHE.

The electrochemical active surface areas (ECSA) were obtained by double layer capacitance ( $C_{\text{dl}}$ ) method where cyclic voltammetry (CV) curves were recorded with a sweep rate of  $20$ – $120 \text{ mV s}^{-1}$  at  $0.80$ – $0.90 \text{ V}$  vs RHE for OER and  $0.77$ – $0.87 \text{ V}$  vs RHE for HER.

#### 2.8. Fabrication of AEMWE system

The AEMWE system consists of a membrane, bipolar plates (BPPs), current collector, gas diffusion layer (GDL) and catalyst layer (CL), which has an active area of  $25 \text{ cm}^2$ . The BPPs, made of titanium, also serve as a current collector and have a serpentine flow channel installed in their center to transport electrolyte. The anion exchange membrane (FAA-3-50) is activated by soaking in 0.5 M  $\text{NaCl}$  and 1 M  $\text{KOH}$  for 24 h, respectively. To ensure proper sealing of the device, FEP gaskets with a thickness of 0.2 mm are used, which should be consistent with the thickness of the self-supported integrated electrode used as both GDL and CL to achieve zero-gap contact. For the AEMWE system to produce relatively purified hydrogen gas, an anode electrolyte feed with a flow rate of  $200 \text{ mL min}^{-1}$  is employed. The energy conversion, energy efficiency and economic evaluation (price per gasoline-gallon equivalent (GGE)  $\text{H}_2$ ) were calculated according to the following equations:

$$\text{Energy consumption (kWh/Nm}^3 \text{ H}_2\text{)} = 2 \times F \times V / V_{\text{H}_2} / 3600 / 1000 \quad (2)$$

$$\text{Energy efficiency (\%)} = V_{\text{neutral}} \times \text{Theoretical electricity} / \text{Energy consumption} / 1000 \quad (3)$$

$$\text{Electricity cost (H}_2/\text{kg}) = 1\text{GGE H}_2/\text{H}_2 \text{ production rate} \times \text{Electrolyzer power} \times \text{Electricity bill} \quad (4)$$

$$\text{H}_2 \text{ production rate} = I / (1.602 \times 10^{-19} \text{ C} \times 2) \quad (5)$$

$$\text{Electrolyzer power} = V \times I \quad (6)$$

Where  $F$  represents faraday constant (96,500 C), and  $V$  represents applied voltage.  $V_{\text{H}_2}$  represents the volume of  $\text{H}_2$  under standard conditions.  $V_{\text{neutral}}$  is 1.48 V, and theoretical electricity is  $2390 \text{ A h/m}^3$ . 1GGE  $\text{H}_2$  is 0.997 kg, and Electricity bill is \$ 0.02/kW h.  $I$  represents the current density at the voltage of  $V$ .

### 3. Results and discussion

#### 3.1. Synthesis and characterization of the prepared catalysts

As illustrated in Fig. 1a, the crystalline-amorphous FePi-NiS/NF was synthesized through a fast electrodeposition step of FePi onto NiS arrays. Specifically, commercial nickel foam (NF) acts as a conductive substrate and serves as the nickel source. Then, the dense NiS arrays were in-situ grown on NF by a mild corrosion engineering. This self-growth strategy constructs an electron transfer channel between the substrate and the catalyst, which ensure the high conductivity of catalysts. In addition, the solid connection between the catalyst layer and the substrate by chemical bond ensures the stability of the electrode under industrial current density. Further morphology details of precursors and catalysts were observed through FE-SEM (Fig. 1b-f). After corrosion by  $\text{Na}_2\text{S}$  solution, rough and dense NiS nanorod arrays are generated on the smooth NF surface, which increases the surface area and provides the growth sites for composite arrays. The NiS nanorod exhibits a length of approximately 150 nm with a diameter of approximately 50 nm. Then, a rougher FePi-NiS/NF can be obtained during the subsequent electrodeposition process where FePi exists in the form of nanoparticles. The formation of three-dimensional rough structure effectively increases the exposure of active site and the gap between nanorods is also conducive to gas diffusion, which jointly guarantees excellent performance of catalytic electrode under high current density. Additionally, the high-resolution TEM image in Fig. 1g reveal clear lattice fringes of 0.161 nm and 0.223 nm which are ascribed to (330) and (211) crystal plane of NiS. Notably, no relevant lattice information of FePi has been found, indicating the formation of amorphous structure. Also, the elemental mapping images of FePi-NiS/NF exhibited the uniform distribution of various elements (Fig. 1h-l). Furthermore, in the XRD results of NiS/NF and FePi-NiS/NF (Fig. S1), only diffraction peaks of metal Ni were detected, indicating that there existed disordered domains within the

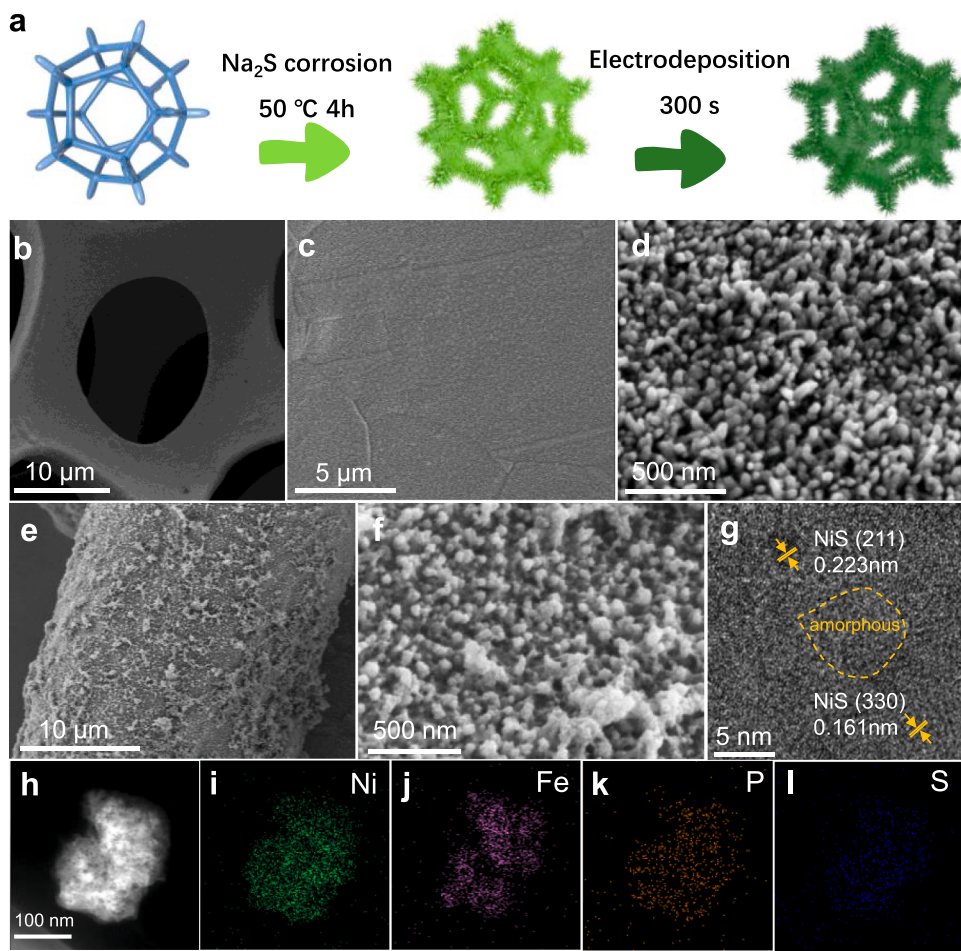


**Fig. 1.** (a) The synthesis process of the FePi-NiS/NF electrocatalysts. SEM images of (b) nickel foam, (c, d) NiS/NF and (e, f) FePi-NiS/NF at different magnifications. (g) HRTEM image and (h-l) elemental mapping images of FePi-NiS/NF.

materials, which is consistent with TEM results. Therefore, it can be confirmed that FePi-NiS/NF arrays was successfully fabricated by a mild two-step approach, which provided feasibility for large-scale preparation of catalysts.

Raman spectra were carried out to further explore the composition and geometric structure of FePi-NiS/NF. As shown in Fig. 2a, the characteristic peak at 192–219 cm<sup>-1</sup> in the Raman spectrum of NiS/NF can be attributed to the E<sub>3</sub> stretching mode of the Ni-S bond in  $\beta$ -NiS, and the characteristic peaks at 300 and 343 cm<sup>-1</sup> can be attributed to the A<sub>1</sub> and E<sub>1</sub> stretching modes of the Ni-S bond [24,25]. Moreover, there are two more Raman peaks in FePi-NiS/NF compared to NiS/NF. The Raman peak located at 475 cm<sup>-1</sup> belongs to the double line stretching vibration mode of (PO<sub>4</sub>)<sup>3-</sup>, and the other at 680 cm<sup>-1</sup> belongs to the vibration peak of the Fe-O bond in FePi [26,27]. In brief, Raman spectra also confirmed the successful synthesis of FePi-NiS/NF composites.

The valence state and electronic interaction of FePi-NiS/NF were further explored by XPS. Firstly, the full spectrum clearly confirms the coexistence of Fe, Ni, P, S and O elements on the surface of FePi-NiS/NF (Fig. 2b). As shown in Fig. 2c, in the high-resolution XPS spectrum of Ni 2p, a pair of characteristic peaks at 855.6 and 873.2 eV belong to Ni<sup>2+</sup> 2p<sub>3/2</sub> and Ni<sup>2+</sup> 2p<sub>1/2</sub>, respectively [28]. The peaks located at 856.7 and 874.3 eV are indexed to the spin orbit splitting of Ni<sup>3+</sup> 2p<sub>3/2</sub> and Ni<sup>3+</sup> 2p<sub>1/2</sub>, and the remaining characteristic peaks are satellite peaks. In the Fe 2p<sub>3/2</sub> XPS spectrum (Fig. 2d), the peaks at 709.5 and 710.8 eV are assigned to the Fe<sup>2+</sup> 2p<sub>3/2</sub> and Fe<sup>3+</sup> 2p<sub>3/2</sub> [29], where the proportion of Fe<sup>2+</sup> is 68.5 %, and the other peak is accompanied satellite peak. As for the high-resolution XPS spectrum of S 2p (Fig. 2e), the characteristic peaks at 162.0 and 168.6 eV were associated with S-M and S-O,

respectively, indicating the presence of NiS and partially oxidized S elements [30]. In the P 2p XPS spectrum (Fig. 2f), the signal peaks of PO<sub>4</sub><sup>3-</sup> and PO<sup>3-</sup> are found at 132.5 and 133.5 eV, respectively, indicating the presence of FePi [31]. More importantly, by comparing the Ni 2p and S 2p XPS spectra of NiS/NF, it could be found that Ni<sup>δ+</sup> 2p<sub>1/2</sub> and 2p<sub>3/2</sub> peaks in FePi-NiS/NF positively shifted by 0.2 eV, while the S-M peak position in S 2p XPS showed a negative shift of 0.9 eV. The above results indicate that there is a strong electronic interaction between composites, causing a higher valence state of Ni<sup>δ+</sup> and electron-enriched S<sup>δ-</sup> in the strongly coupled composites, which has been proved to facilitate the electron transfer [32]. In addition, by comparing the peak areas of S-O and S-M in S 2p, it can be seen that the formation of composites also helps reduce the oxidation of S element, which also guaranteed the long-term stability of the catalysts.

### 3.2. Electrocatalytic OER performance of FePi-NiS/NF

Typically, due to four coupled proton-electron transfer steps, OER shows sluggish reaction kinetics and has become the bottleneck of water electrolysis. The prepared FePi-Ni/NF exhibits excellent OER performance, which can improve the efficiency of hydrogen production. Firstly, the optimal synthesis conditions for FePi-Ni/NF have been investigated, including electrodeposition potential, time, and concentration. The results showed that the optimal deposition potential was -1.4 V and the optimal deposition time was 300 s (Fig. S2a,b). It is worth noting that the introduction of trace amounts of FePi can effectively enhance the OER activity of NiS (Fig. S2c). As shown in Fig. 3a, the polarization curve of FePi-NiS/NF was tested in comparison with FePi/NF, NiS/NF and IrO<sub>2</sub>. It

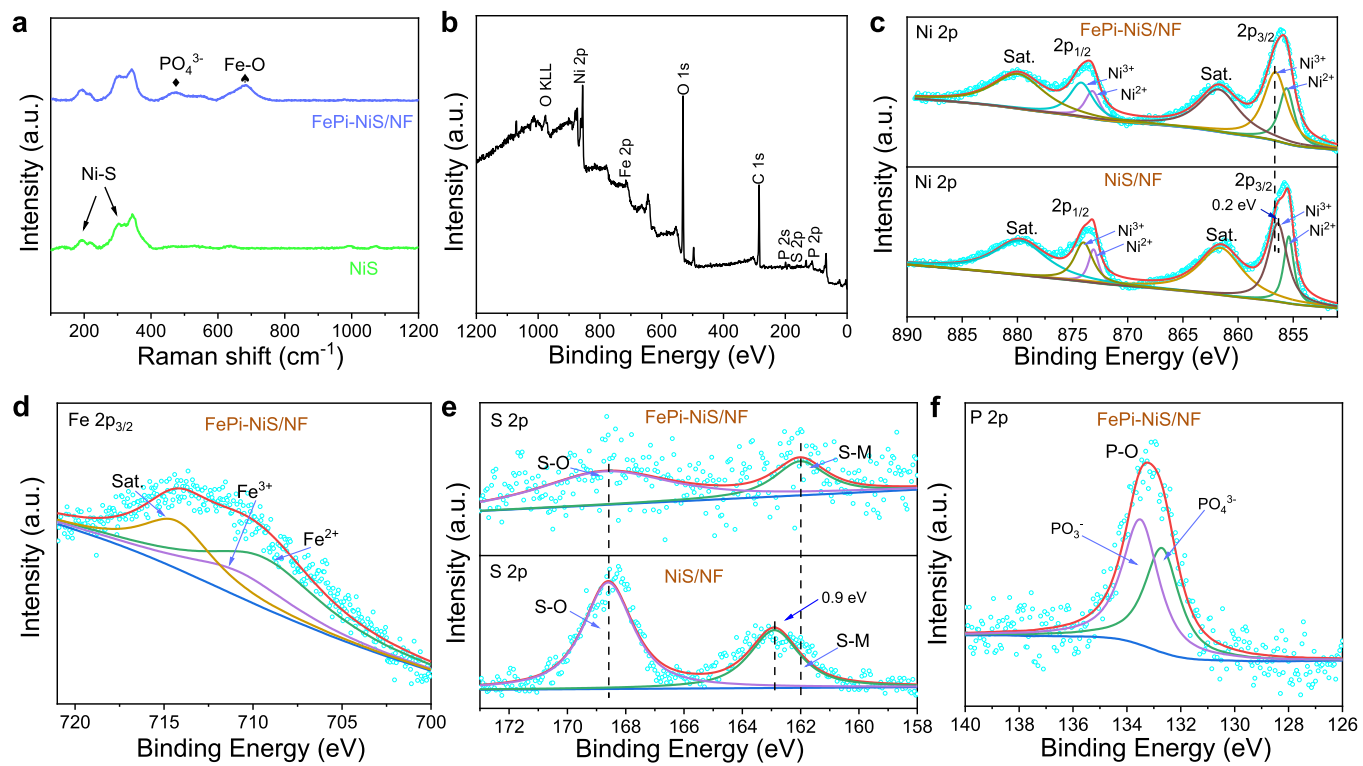


**Fig. 2.** (a) Raman spectra of FePi-NiS/NF and NiS/NF. (b) XPS survey of FePi-NiS/NF. High-resolution XPS spectra of (c) Ni 2p, (d) Fe 2p, (e) S 2p and (f) P 2p.

can be observed that FePi-NiS/NF exhibits the best activity within full voltage range. Remarkably, for FePi-NiS/NF, the high current densities of 100, 500, and 1000  $\text{mA cm}^{-2}$  can be reached at only 262, 307, and 345 mV, respectively, which is far superior to FePi/NF (298 mV @ 100  $\text{mA cm}^{-2}$ , 352 mV @ 500  $\text{mA cm}^{-2}$ , 399 mV @ 1000  $\text{mA cm}^{-2}$ ), NiS/NF (308 mV @ 100  $\text{mA cm}^{-2}$ , 358 mV @ 500  $\text{mA cm}^{-2}$ , 409 mV @ 1000  $\text{mA cm}^{-2}$ ) and commercial  $\text{IrO}_2/\text{NF}$  (365 mV @ 100  $\text{mA cm}^{-2}$ , 427 mV @ 500  $\text{mA cm}^{-2}$ , 454 mV @ 1000  $\text{mA cm}^{-2}$ ) (Fig. 3b). The results indicate that the synergistic effect between composites results in much higher performance of FePi-NiS/NF than FePi/NF and NiS/NF.

Further analyses were conducted on the Tafel slope, electrochemical resistance, and electrochemical active surface area to further confirm the superiority of composite arrays. Specifically, the lowest Tafel slope of FePi-NiS/NF (41.5 mV  $\text{dec}^{-1}$ ) was achieved compared to FePi/NF (46.2 mV  $\text{dec}^{-1}$ ), NiS/NF (45.6 mV  $\text{dec}^{-1}$ ), and  $\text{IrO}_2/\text{NF}$  (58.6 mV  $\text{dec}^{-1}$ ), indicating the faster catalytic kinetics (Fig. 3c). As shown in Fig. 3d, FePi-NiS/NF exhibited the lowest charge transfer resistance in comparison with FePi/NF and NiS/NF, indicating the faster charge transfer during the reaction process. Furthermore, ECSA was calculated through double-layer capacitance ( $C_{dl}$ ) to estimate the accessible active sites (Fig. 3e and Fig. S3). The highest  $C_{dl}$  (0.84  $\mu\text{F cm}^{-2}$ ) and ECSA (21.0  $\text{cm}^2$ ) of FePi-NiS/NF revealed the more exposed active area compared with FePi/NF (0.43  $\mu\text{F cm}^{-2}$ , 10.8  $\text{cm}^2$ ) and NiS/NF (0.35  $\mu\text{F cm}^{-2}$ , 8.8  $\text{cm}^2$ ). Moreover, the higher ECSA-normalized current density of FePi-NiS/NF indicates the supreme intrinsic activity which may due to the optimized electronic structure of composites (Fig. 3f). The above results confirmed that FePi-NiS/NF possesses superior charge transfer ability, faster reaction kinetics and abundant active sites, resulting in outstanding performance at industrial current densities. Notably, FePi-NiS/NF also exhibits superior activity to the most excellent catalysts in the previous reports (Fig. 3g). In addition, chronoamperometry was carried out to evaluate the stability of the catalyst at industrial current density. As shown in Fig. 3h, at a high current density of 1000  $\text{mA cm}^{-2}$ , only 1.1 % decline was observed within 500 h, demonstrating the excellent stability of FePi-NiS/NF for industrial applications.

### 3.3. Discussion of the active site for OER

It is reported that the catalysts always undergo in-situ reconstruction during the OER process to generate truly active species [33]. Due to the good stability of FePi-NiS/NF and to ensure the sufficient reconstruction of the catalyst, we selected samples after stability testing to characterize its active species under industrial current density. Firstly, the valence state transition of active species was analyzed by XPS spectra. As shown in Fig. 4a, the XPS spectrum of Fe 2p<sub>3/2</sub> showed that all  $\text{Fe}^{2+}$  transformed into  $\text{Fe}^{3+}$  during OER, while the Ni 2p XPS spectrum did not show significant changes (Fig. 4b). Besides, the leaching of P and S elements could be observed from the XPS spectra of P 2p and S 2p (Fig. 4c-d). It can be reasonably speculated that the dissolution of P and S during the OER induced catalyst reconstruction and the transition of valence states. Furthermore, the high-resolution spectrum of O 2p after OER showed two more XPS peaks located at 529.3 and 530.6 eV, which could be attributed to reactive oxygen species ( $\text{O}_2^{\cdot}/\text{O}^-$ ) and oxygen vacancies ( $\text{O}_v$ ) (Fig. 4e) [34–36]. To further explore the structure of active species, post-reaction Raman spectrum was conducted that the  $\text{Ni}^{3+}$  and  $\text{Fe}^{3+}$  species formed after OER are  $\text{NiOOH}$  (464 and 545  $\text{cm}^{-1}$ ) and  $\text{FeOOH}$  (571 and 675  $\text{cm}^{-1}$ ) (Fig. 4f) [37–39]. Interestingly, the Raman peaks of NiS and FePi still seemed to exist, indicating incomplete reconstruction of FePi-NiS/NF, which ensured the high conductivity and stability of catalyst. Meanwhile, HRTEM image (Fig. 4g) displayed the interplanar spacing of 0.219 nm and 0.225 nm corresponded to the (104) plane of  $\alpha\text{-NiOOH}$  and the (121) plane of  $\text{FeOOH}$ , respectively, which were consistent with results of Raman spectra. Furthermore, it can be seen that the tightly connected nanosheet array was formed after OER (Fig. 4h), which constructed thin-walled sponge like pores with the size of approximately 150–200 nm, conducive to bubble diffusion. The above characterizations showed that FePi-NiS/NF partly reconstructed into active species  $\text{O}_v\text{-NiOOH}/\text{FeOOH}$  under high OER current density due to the leaching of P and S (Fig. 4i). It has been reported that the presence of oxygen vacancies can enhance the intrinsic conductivity of  $\text{NiOOH}$  and  $\text{FeOOH}$ , improve the charge transfer, and activate super-oxo/peroxo like  $\text{O}_2^{\cdot}/\text{O}^-$  (typically e.g.  $\text{NiOO}^{\cdot}$ ) which has also been

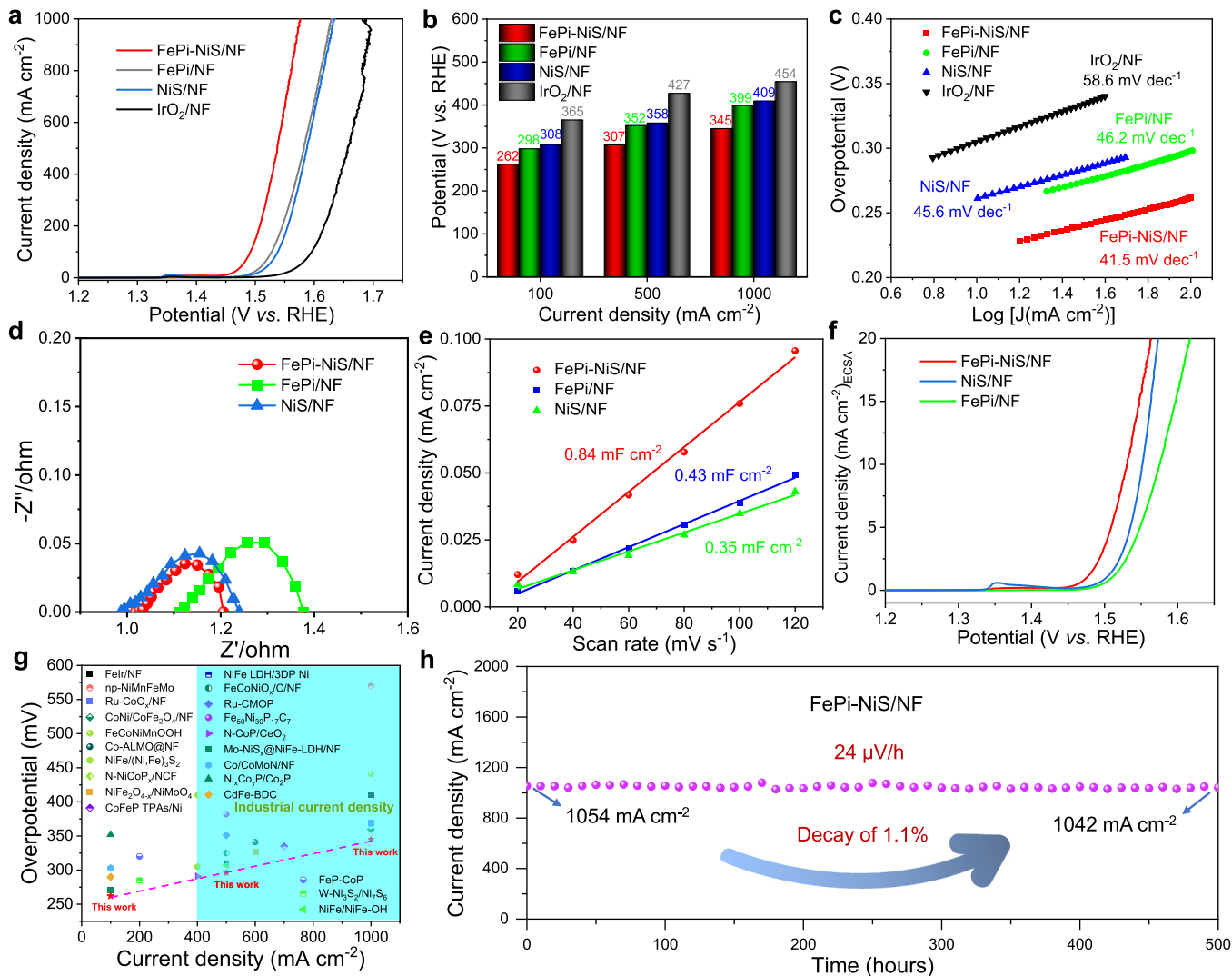


**Fig. 3.** (a, b) OER performance and (c) corresponding Tafel plots of FePi-NiS/NF, FePi/NF, NiS/NF and IrO<sub>2</sub>/NF. (d) EIS Nyquist plots, (e) C<sub>dl</sub> values, and (f) ECSA-normalized polarization curves of FePi-NiS/NF, FePi/NF and NiS/NF. (g) Performance comparison with reported excellent catalysts in the literature. (h) Stability test of FePi-NiS/NF at 1.58 V.

detected in the above XPS [40–42]. Notably, the highly oxidative O<sub>2</sub><sup>2-</sup>/O<sup>-</sup> species formed on the surface catalysts are confirmed to accelerate OER kinetics in alkaline solution [43]. We further investigated the role of amorphous FePi by quasi in-situ Raman spectra for samples tested at different voltages (Fig. S4). For NiS/NF, the characteristic peaks of Ni(OH)<sub>2</sub> were detected, while the peak of NiOOH was not obvious due to its instability. For FePi-NiS/NF, as the test voltage increases (> 1.4 V), it is evident that the signal peaks of NiOOH can stably exist. Therefore, we speculate that the amorphous FePi can be reconstructed into FeOOH to enhance overall activity while stabilizing NiOOH species, which is consistent with the literature results [44].

### 3.4. Electrocatalytic HER performance of NiCoPi-NiS/NF

Using non-noble metal catalyst instead of Pt/C for HER is still important in reducing commercial costs. However, FePi-NiS/NF exhibited unsatisfactory activity in HER (Fig. S5a). In order to verify the universality of the synthesis strategy, we further prepared high-performance HER catalyst NiCoPi-NiS/NF, although its OER performance is not as good as that of FePi-NiS/NF (Fig. S5b). Different from FePi-NiS/NF, NiCoPi-NiS/NF exhibits drum like structure (Fig. S6). As shown in Fig. S7a, HRTEM clearly showed the crystal plane spacing of

0.161 nm and 0.223 nm, corresponding to NiS (211) and (311). Moreover, the phosphate existed in an amorphous form, consistent with the XRD results (Fig. S7b). Besides, the elements are evenly distributed in catalyst, providing conditions for the scaling up of catalyst (Fig. S7c-g). Surface sensitive Raman spectrum were further conducted to explore the composition and geometric structure of NiCoPi-NiS/NF (Fig. S8). It can be observed that the Raman peaks at 189 and 300 cm<sup>-1</sup> of Ni-S still exist, while the newly formed peaks at 514 and 660 cm<sup>-1</sup> belonged to the octahedral stretching vibration signal peaks of Co-O and NiO<sub>6</sub> in nickel/cobalt phosphate [45,46]. Additionally, the Raman peaks at 463 and 951 cm<sup>-1</sup> could be attributed to the symmetric stretching vibration modes of O-P-O (double line) and (PO<sub>4</sub>)<sup>3-</sup> (single line), respectively [47]. Therefore, the above characterizations confirm the successful preparation of a crystalline-amorphous NiCoPi-NiS/NF composite electrode.

The XPS full spectrum of NiCoPi-NiS/NF clearly confirmed the coexistence of Co, Ni, P, S, and O (Fig. S9a). In the Ni 2p XPS spectrum (Fig. S9b), a pair of characteristic peaks at 855.9 and 873.5 eV belonged to Ni<sup>2+</sup> 2p<sub>3/2</sub> and Ni<sup>2+</sup> 2p<sub>1/2</sub>, respectively, while the other two peaks at 857.0 and 874.6 eV corresponded to the Ni<sup>3+</sup> 2p<sub>3/2</sub> and Ni<sup>3+</sup> 2p<sub>1/2</sub>, indicating that Ni<sup>6+</sup> in NiCoPi-NiS/NF exists in the form of +2 and +3 valence. In the Co 2p XPS spectrum (Fig. S9c), the characteristic peaks at

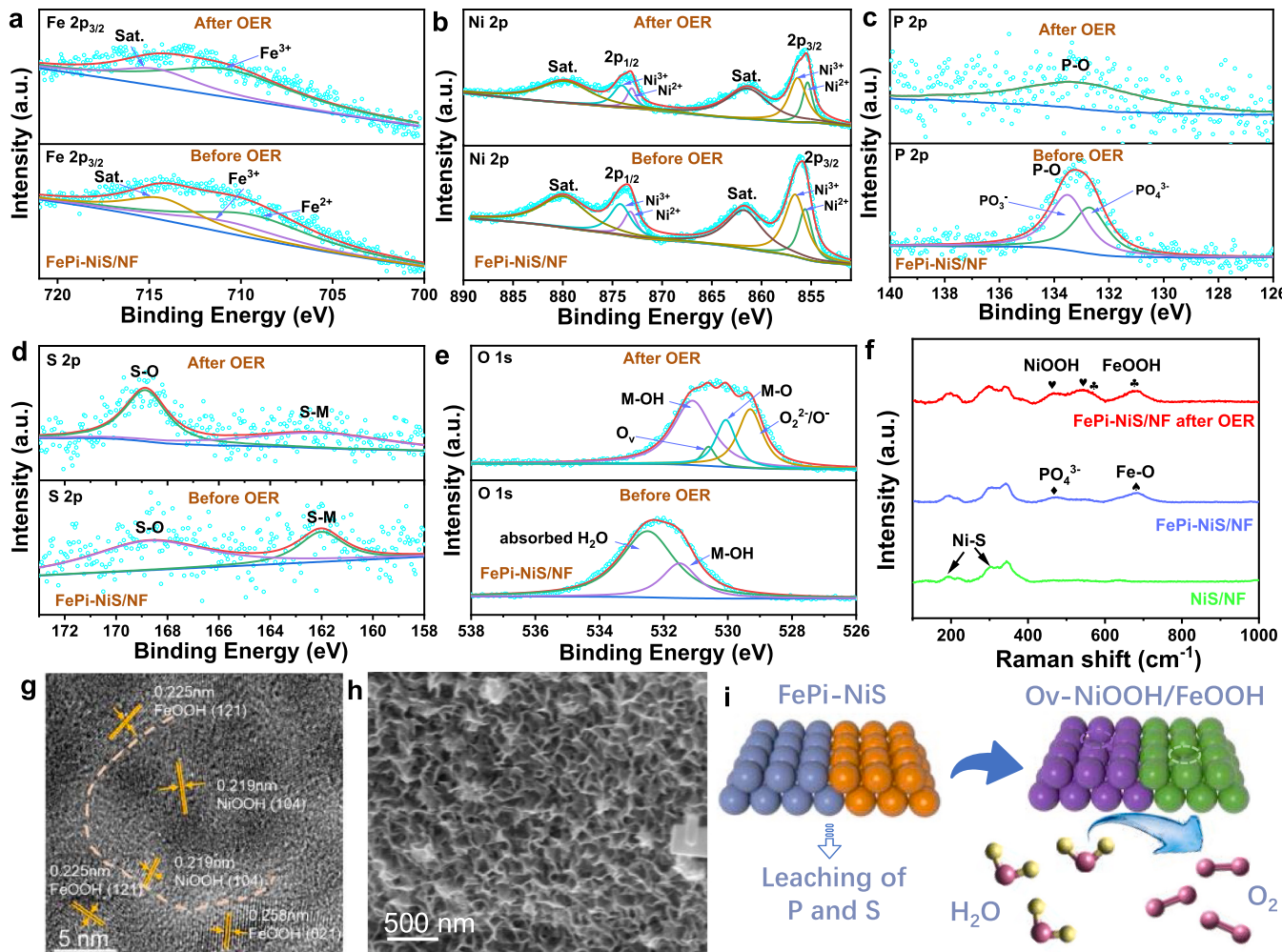


**Fig. 4.** The characterizations of FePi-NiS/NF after OER stability testing. (a-e) High-resolution XPS spectra of Fe 2p, Ni 2p, P 2p, S 2p and O 1 s (e) Raman spectra. (f) HRTEM image. (g) FE-SEM image. (h) Schematic illustration of OER process.

782.1 and 798.1 eV can be assigned to  $\text{Co}^{2+}$  2p<sub>3/2</sub> and  $\text{Co}^{2+}$  2p<sub>1/2</sub>, respectively, indicating that the Co element in the catalyst exists in the form of + 2 valence [48]. The signal of S-M and S-O located at 162.6 and 169.3 eV in S 2p XPS spectrum (Fig. S9d) further revealed the presence of NiS [30]. Besides, in the high-resolution spectrum P 2p (Fig. S9e), the peaks at 132.5 and 133.3 eV of  $\text{PO}_4^{3-}$  and  $\text{PO}_3^-$  also confirmed the presence of NiCoPi [31]. Furthermore, by comparing with NiS/NF, a positive binding energy shift by 0.4 eV was found for  $\text{Ni}^{\delta+}$  2p in NiCoPi-NiS/NF, while the position of S-M peak in S 2p XPS showed a negative shift by 0.3 eV. The results revealed a strong electronic interaction between composites, where more electrons were transferred from  $\text{Ni}^{3+}$  to  $\text{S}^{\delta-}$ , enhancing the ability to accept protons of  $\text{S}^{\delta-}$  during catalytic processes.

The electrochemical HER performance of NiCoPi-NiS/NF was comprehensively explored. Firstly, the optimal preparation conditions were screened by adjusting the feeding ratio ( $\text{NiCl}_2$ :  $\text{CoCl}_2$  = 3:1), deposition voltage (-1.6 V), and deposition time (300 s) (Fig. S10). As shown in Fig. 5a-b, among the catalysts, commercial Pt/C/NF electrodes exhibited high activity at low current density (81 mV @  $-100 \text{ mA cm}^{-2}$ ), while 111, 152, and 297 mV were required for NiCoPi-NiS/NF, NiCoPi NF, and NiS/NF, respectively. However, NiCoPi-NiS/NF exhibits tremendous advantage under high current densities, where  $-500$  and  $-1000 \text{ mA cm}^{-2}$  can be reached with a ultra-low potential of 174 and 223 mV, respectively, far superior to Pt/C/NF (231 mV @  $-500 \text{ mA cm}^{-2}$ , 375 mV @  $-1000 \text{ mA cm}^{-2}$ ), NiCoPi/NF (237 mV @  $-500 \text{ mA cm}^{-2}$ , 302 mV @  $-1000 \text{ mA cm}^{-2}$ ), and NiS/NF (444 mV @

$-500 \text{ mA cm}^{-2}$ , 500 mV @  $-1000 \text{ mA cm}^{-2}$ ). The above results indicated a beneficial electronic interaction between composites, resulting in a remarkable activity of NiCoPi-NiS/NF superior to NiCoPi/NF and NiS/NF over the full voltage range. In addition, the curve fluctuation of Pt/C/NF electrode under high current density reflected that hydrogen cannot be desorbed timely due to the presence of binder, resulting in poor catalytic activity compared to self-supported electrodes. Moreover, a low Tafel slope of NiCoPi-NiS/NF (53.1 mV dec<sup>-1</sup>) suggested the faster reaction kinetics in comparation with NiCoPi/NF (69.2 mV dec<sup>-1</sup>) and NiS/NF (122.0 mV dec<sup>-1</sup>) (Fig. 5c). In addition, benefiting from synergistic effect between composites, NiCoPi-NiS/NF also exhibited the lowest charge transfer resistance (Fig. 5d), which is conducive for reducing the electrochemical active surface area of the catalyst was measured by the  $C_{dl}$  method (Fig. S11). The results showed that NiCoPi-NiS/NF had the largest  $C_{dl}$  (1.34 mF  $\text{cm}^{-2}$ ) and ECSA (33.5  $\text{cm}^2$ ) (Fig. 5e), indicating the more exposed active sites of NiCoPi-NiS/NF. Moreover, ECSA-normalized current density confirms the highest intrinsic activity of NiCoPi-NiS/NF (Fig. 5f). Remarkably, the activity of NiCoPi-NiS/NF exceeds that of most reported advanced HER catalysts (Fig. 5g). The stability of the catalyst at industrial current density was evaluated by chronoamperometry method. As shown in Fig. 5h, only 0.5 % decay of activity was observed within 400 h at a high current density of  $1000 \text{ mA cm}^{-2}$ , demonstrating the potential for industrial applications.

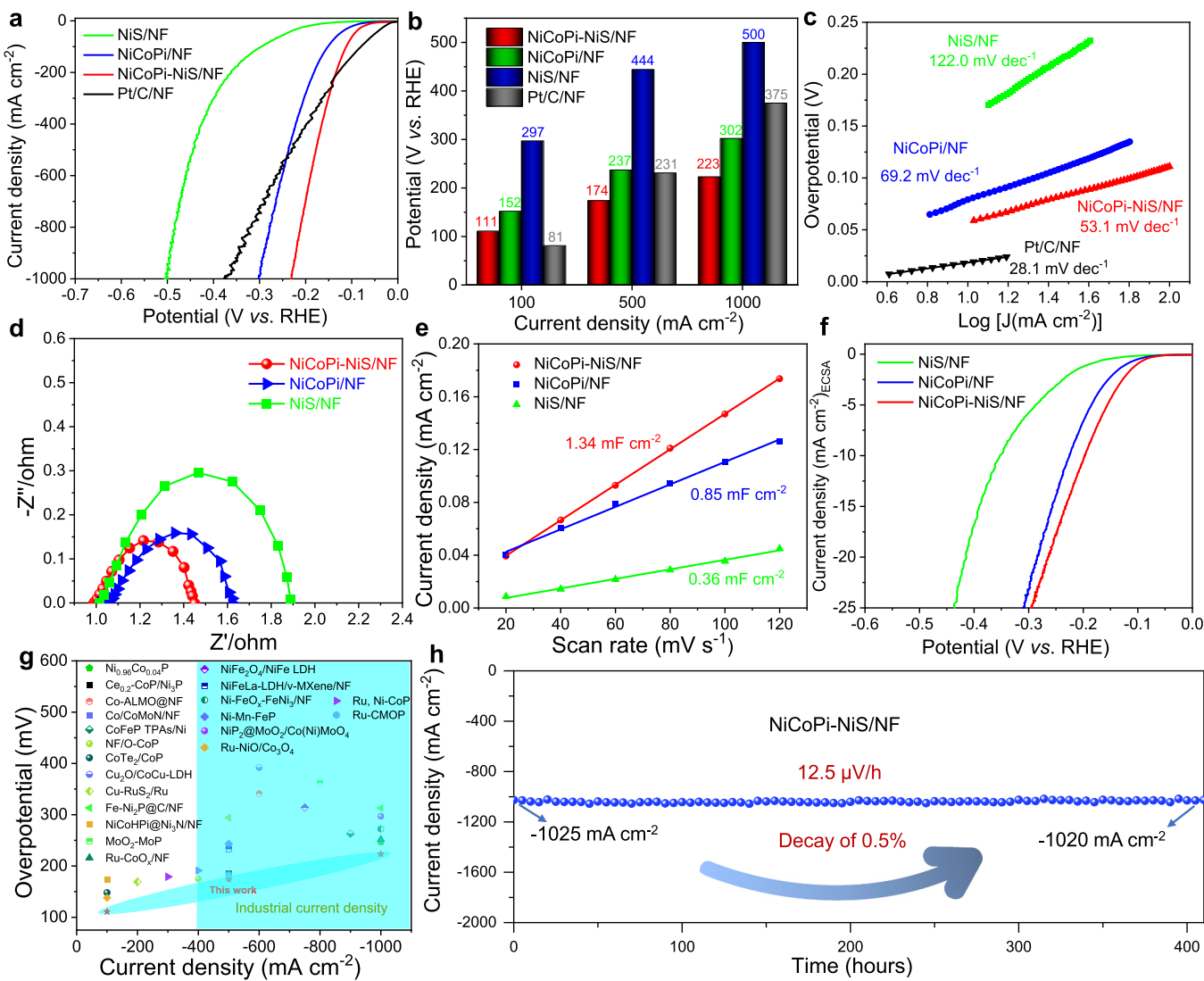


**Fig. 5.** (a, b) HER performance and (c) corresponding Tafel plots of NiCoPi-NiS/NF, NiCoPi/NF, NiS/NF and Pt/C/NF. (d) EIS Nyquist plots, (e)  $C_{dl}$  values, and (f) ECSA-normalized polarization curves of NiCoPi-NiS/NF, NiCoPi/NF and NiS/NF. (g) Performance comparison with reported excellent catalysts in the literature. (h) Stability test of FePi-NiS/NF at  $-0.223$  V.

### 3.5. Discussion of the active site for HER

Recently, few reports found that catalysts may undergo reconstruction during the HER process. At a certain reduction current density, the breaking of M-S bonds and the attack of hydroxyl groups lead to the reconstruction of sulfides into hydroxides [49]. For Ni-based catalysts, due to the potential range of HER has a certain overlap with  $\varphi$  (Ni ( $\text{OH}_2$ )/Ni), Ni( $\text{OH}_2$ ) may form during HER process, which can accelerate the kinetics of water splitting, and similar reconstruction behavior also exists in Co-based catalysts [50,51]. However, the active species under industrial current density still need to be explored to further provide guidance for the design of commercial catalysts. Firstly, the post-reaction XPS was performed to investigate the valence state of active species. As shown in Fig. S12a, the Co 2p XPS spectrum showed that the Co element still existed with  $+2$  valence. Moreover, the binding energies of Co 2p peaks positively shifted by  $1.0$  eV compared with that before HER, indicating an electron-rich state of  $\text{Co}^{2+}$ . Besides, it can be observed in Ni 2p XPS (Fig. S12b) that a large number of  $\text{Ni}^{2+}$  species were generated after HER, and the proportion of  $\text{Ni}^{2+}$  increased from  $44.1\%$  to  $89.0\%$ . In addition, both P 2p and S 2p XPS spectra indicated a significant leaching of P and S in alkaline solution under high current density (Fig. S12c-d). Notably, a large number of hydroxides were

observed in post-reaction O 1s XPS that the proportion of  $\text{OH}^-$  increased from  $28.2\%$  to  $85.7\%$  after HER (Fig. S12e). Furthermore, it was found that the peak intensity at  $450\text{--}520\text{ cm}^{-1}$  in Raman spectra was significantly enhanced, which can be attributed to  $\beta\text{-Ni(OH)}_2$  [52], while the characteristic peak at  $\sim 560\text{ cm}^{-1}$  can be attributed to disordered or defective  $\text{Ni(OH)}_x$  (Fig. S13a) [53]. Besides, another signal of  $\text{Co(OH)}_2$  was also found at  $1053\text{ cm}^{-1}$  (Fig. S13a) [54]. Accordingly, the lattice stripes of  $\text{Co(OH)}_2$  (011) and  $\text{Ni(OH)}_2$  (100) can be identified in HRTEM (Fig. S13b). The above characterizations jointly confirmed the reconstruction of NiCoPi-NiS/NF into electron-rich  $\text{Co(OH)}_2$  and  $\beta\text{-Ni(OH)}_2$  active species during HER, due to the leaching of P and S in alkaline solution under industrial current density. It has been reported that both  $\text{Ni(OH)}_2$  and unsaturated  $\text{Co(OH)}_2$  with low valence state are beneficial for water dissociation, leading to an improved dynamics of Volmer step which is also consistent with our Tafel slope results [51,55]. The morphological changes after HER were observed by FE-SEM that the sheet structure with open exhaust channels was constructed, where more active sites can be exposed (Fig. S13c-d). We further investigated the role of amorphous NiCoPi by quasi in-situ Raman spectra for samples tested at different voltages (Fig. S14). In detail, NiS is relatively stable under negative voltage, but there still exists a small amount of  $\text{Ni(OH)}_2$  whose peak position shifts positively as the voltage decreases, which is

considered to be the formation of disordered  $\text{Ni(OH)}_x$  [53]. For  $\text{NiCoPi-NiS/NF}$ , the dissolution of phosphate triggers surface reconstruction to generate Nickel hydroxide species, and the signal peak of  $\text{Co(OH)}_2$  can be detected at  $-0.3$  V. Therefore,  $\text{NiCoPi}$  promotes the generation of surface  $\text{Ni(OH)}_x$  and active  $\text{Co(OH)}_2$  species. Based on the above analysis, the special electron structure and morphology of the active species ensure the excellent HER performance under industrial current density.

### 3.6. Electrocatalytic performance for overall water splitting

In view of the remarkable HER and OER performance for composite electrodes, overall water splitting was performed with  $\text{NiCoPi-NiS/NF} \parallel \text{FePi-NiS/NF}$  in a two-electrode system. As shown in Fig. 6a, the current densities 100, 500, and  $1000 \text{ mA cm}^{-2}$  can be reached with the cell voltages of only  $1.664$ ,  $1.763$ , and  $1.824$  V, respectively in  $1 \text{ M KOH}$  at  $25^\circ\text{C}$ , far superior to commercial  $\text{Pt/C/NF} \parallel \text{IrO}_2/\text{NF}$  ( $1.882 \text{ V} @ 500 \text{ mA cm}^{-2}$ ). Notably, when the temperature raised to  $50$  and  $70^\circ\text{C}$ , the lower voltages of  $1.762$  and  $1.735$  V were required to reach  $1000 \text{ mA cm}^{-2}$ , exhibiting improved kinetics at high temperature (Fig. S15). In addition, the activity of prepared catalysts under simulated industrial conditions were further evaluated. In  $6 \text{ M KOH}$  at  $70^\circ\text{C}$ , a high current density of  $1000 \text{ mA cm}^{-2}$  was achieved at an ultra-low voltage of only  $1.712$  V, while  $1.886$  V was required to reach  $1000 \text{ mA cm}^{-2}$  for commercial catalysts (Fig. 6b). Remarkably, the performance of our electrode pairs exceeds the excellent catalysts reported in literature under industrial current densities (Fig. 6c and Table S1). In addition, the stability of the two-electrode system at high current density was tested using chronoamperometry method that there was almost no decline of current density within  $200 \text{ h}$  (from  $1046 \text{ mA cm}^{-2}$  to  $1037 \text{ mA cm}^{-2}$ ) (Fig. 6d), confirming the remarkable stability performance of catalysts. In brief, all the results indicated that

the composite electrode is a promising substitute for commercial catalysts.

More importantly,  $\text{NiCoPi-NiS/NF} \parallel \text{FePi-NiS/NF}$  also exhibited impressive performance in other electrochemical systems, expected to further achieve green hydrogen production with low energy consumption. Specifically, in simulated seawater ( $1 \text{ M KOH} + 0.5 \text{ M NaCl}$ ), a current density of  $1000 \text{ mA cm}^{-2}$  can be achieved with only  $1.86 \text{ V}$  at room temperature (Fig. S16a). Furthermore, the lower voltages of  $1.80$  and  $1.75 \text{ V}$  were required with the temperature rising to  $50$  and  $70^\circ\text{C}$ . Interestingly, the above performance is very close to that of OER, indicating that the chloride ion environment has a weak impact on the catalyst [56]. In addition, the long-term stability under industrial current density was tested that the current density declined from  $982 \text{ mA cm}^{-2}$  to  $961 \text{ mA cm}^{-2}$  within  $250 \text{ h}$  with a decrease of only  $2.1\%$ , demonstrating its high resistance to chloride ion corrosion (Fig. S16b). Additionally, integrating HER and sulfide oxidation reaction (SOR) is expected to achieve both reduced energy consumption for hydrogen production and purification of sulfur-rich wastewater. So, the performance of  $\text{NiCoPi-NiS/NF} \parallel \text{FePi-NiS/NF}$  for  $\text{S}^{2-}$  degradation was investigated. As shown in Fig. S17a, in  $1 \text{ M KOH}$  with  $0.5 \text{ M Na}_2\text{S}$ , the voltages of only  $0.74$  and  $0.91 \text{ V}$  were required at room temperature to reach  $100$  and  $300 \text{ mA cm}^{-2}$ , respectively, which is  $930$  and  $820 \text{ mV}$  lower than water electrolysis, greatly reducing the energy consumption. In addition, we also confirmed the degradation product of value-added  $\text{S}_8$  through XRD (Fig. S17b). One the other hand,  $\text{NiCoPi-NiS/NF} \parallel \text{FePi-NiS/NF}$  also exhibited excellent urea oxidation (UOR) performance in a  $1 \text{ M KOH} + 0.5 \text{ M CO(NH}_2\text{)}_2$  electrolyte (Fig. S18), where a current density of  $500 \text{ mA cm}^{-2}$  can be obtained at  $1.70 \text{ V}$ , demonstrating the potential for electrolysis of industrial urea-rich wastewater. Our catalysts exhibited comparable performance to excellent catalysts in the above electrochemical systems (Table S2), demonstrating the broad application prospects.

### 3.7. Electrocatalytic performance for AEMWE

In order to further confirm the potential of our catalysts for industrial application, a preliminary amplification of the electrodes was conducted. Specifically,  $5 \times 5 \text{ cm}^2$  scale self-supported electrodes were successfully prepared with a uniform surface, assembled in scaled-up AEMWE (Fig. 7a and Fig. S19). It should be noted that no high energy consumption technology is required during the preparation process, greatly saving industrial costs. In order to simulate actual industrial condition, the anode feeding style was selected to reduce the cost of hydrogen drying.

Firstly, the optimized flow rate ( $200 \text{ mL min}^{-1}$ ) was selected by testing the performance of commercial catalysts at different flow rates (Fig. S20a). Then, the performance of AEMWE at room temperature and industrial operating temperature was investigated. As shown in Fig. S20b, at room temperature, a voltage of  $2.19 \text{ V}$  was required to reach a high current of  $25 \text{ A}$  for  $\text{NiCoPi-NiS/NF} \parallel \text{FePi-NiS/NF}$ , far exceeding that of commercial  $\text{Pt/C/NF} \parallel \text{IrO}_2/\text{NF}$  ( $2.52 \text{ V} @ 25 \text{ A}$ ). As the temperature raised to  $50^\circ\text{C}$ , a current of  $12.5$  and  $25.0 \text{ A}$  can be achieved by applying only  $1.87$  and  $2.10 \text{ V}$  for  $\text{NiCoPi-NiS/NF} \parallel \text{FePi-NiS/NF}$ , still showing surpassing activity than commercial  $\text{Pt/C/NF} \parallel \text{IrO}_2/\text{NF}$  ( $1.96 \text{ V} @ 12.5 \text{ A}$ ,  $2.28 \text{ V} @ 25.0 \text{ A}$ ) (Fig. 7b, c). Furthermore, there was no decay of current for  $30 \text{ h}$  under operating conditions of  $50^\circ\text{C}$  and  $12.5 \text{ A}$  (area:  $\approx 25 \text{ cm}^2$ ), showing outstanding stability under harsh industrial condition better than commercial  $\text{Pt/C/NF} \parallel \text{IrO}_2/\text{NF}$  (Fig. 7d and Fig. S21). Remarkably, the high energy efficiency of  $70.5\%$  and  $79.2\%$  can be obtained under the high current of  $25.0$  and  $12.5 \text{ A}$  (Fig. 7d). In addition, the self-made catalysts exhibit a reduced voltage of  $90$  and  $180 \text{ mV}$  compared to commercial catalysts at  $12.5$  and  $25.0 \text{ A}$ , meaning that the electricity consumption of  $0.215 \text{ kWh}$  and  $0.43 \text{ kWh}$  can be saved when generating hydrogen gas per standard cubic meter (Fig. 7e). Moreover, the performance of assembled AEMWE system can also be comparable to those in literature (Fig. 7f and Table S3). The

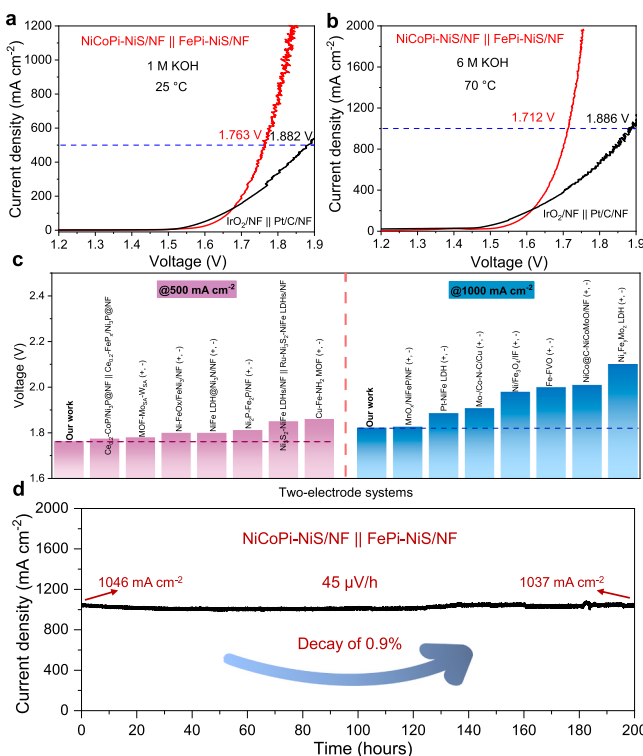


**Fig. 6.** Two-electrode tests of  $\text{NiCoPi-NiS/NF} \parallel \text{FePi-NiS/NF}$  and  $\text{Pt/C/NF} \parallel \text{IrO}_2/\text{NF}$  at (a)  $25^\circ\text{C}$  in  $1 \text{ M KOH}$  and (b)  $70^\circ\text{C}$  in  $6 \text{ M KOH}$ . (c) Performance comparison with reported excellent catalysts in the literature at  $500 \text{ mA cm}^{-2}$  and  $1000 \text{ mA cm}^{-2}$  (d) Stability test of  $\text{NiCoPi-NiS/NF} \parallel \text{FePi-NiS/NF}$  at  $1.83 \text{ V}$  vs. RHE.

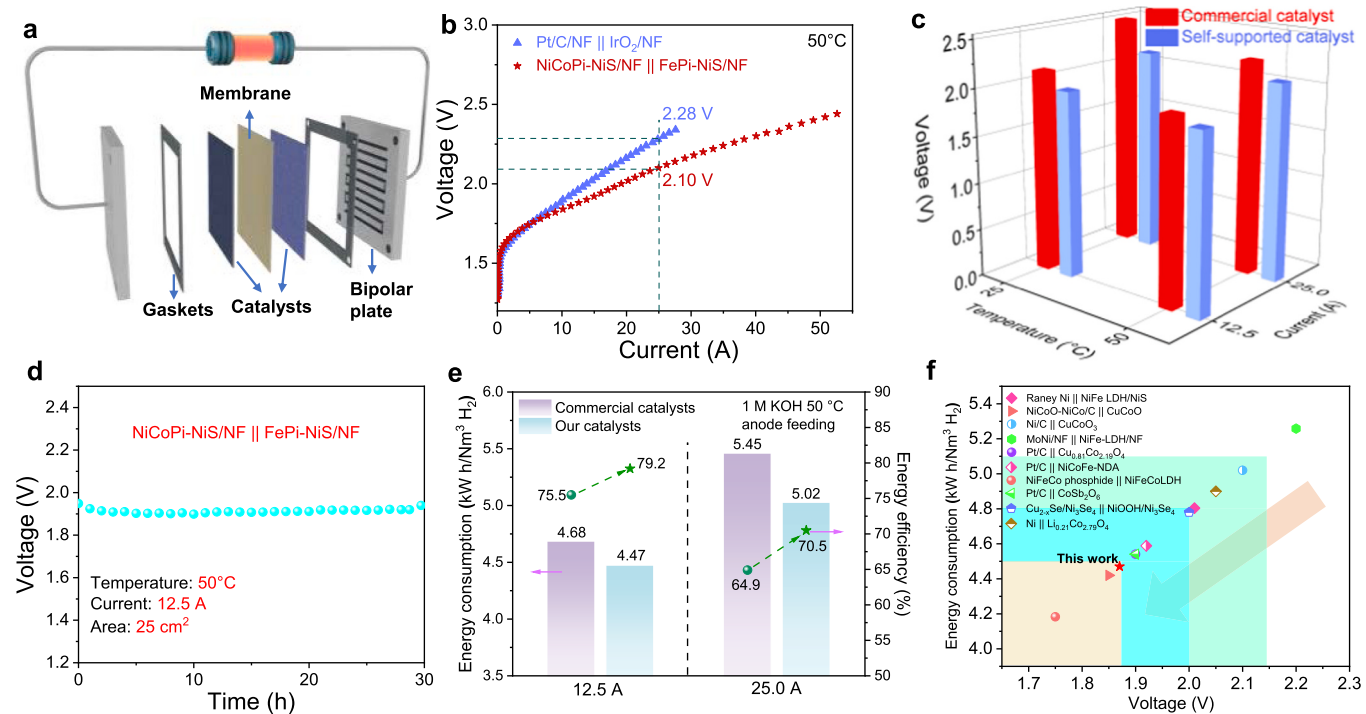


**Fig. 7.** (a) Schematic assembly of AEMWE. (b) Polarization curve of AEMWE tests of NiCoPi-NiS/NF || FePi-NiS/NF and commercial Pt/C/NF || IrO<sub>2</sub>/NF at 50 °C (without iR-correction). (c) Performance comparison of commercial catalysts and self-supported catalysts at different temperature. (d) Stability test of NiCoPi-NiS/NF || FePi-NiS/NF under operating conditions of 50 °C and 12.5 A (area:  $\approx 25 \text{ cm}^2$ ). (e) Comparison of energy consumption and efficiency values between our catalysts and commercial catalysts. (f) Comparison of the NiCoPi-NiS/NF || FePi-NiS/NF with the reported catalysts applied in AEMWE.

calculated price per gallon of gasoline equivalent (GGE) of the H<sub>2</sub> produced is as low as \$ 1.00 and \$ 1.12 at 12.5 and 25.0 A respectively, which is less than the target of \$ 2.00 by 2026 from the U.S. DOE [57]. In brief, our NiCoPi-NiS/NF || FePi-NiS/NF electrode exhibits the advantages of low cost, easy scaling up, and high performance, which has been demonstrated to be a feasible catalyst for industrial hydrogen production.

#### 4. Conclusion

We have developed composite electrodes of MPi-NiS/NF (M=Fe, Co, Ni) by a facile and mild method. The unique crystalline-amorphous structure of the electrodes promotes the OER and HER dynamics, respectively, via the partial reconstruction of catalysts under high current density, resulting in the formation of O<sub>v</sub>-NiOOH/FeOOH and Co (OH)<sub>2</sub>/Ni(OH)<sub>2</sub>. Meanwhile, the electrodes have a reconstructed nanosheet with a pore structure that is beneficial to the exposure of abundant active sites and bubble diffusion. Consequently, FePi-NiS/NF requires only 345 mV, and NiCoPi-NiS/NF requires only 223 mV to achieve a current density of 1000 mA cm<sup>-2</sup> under alkaline conditions. These composite electrodes demonstrate outstanding performance under industrial conditions (6 M KOH, 70 °C), requiring only 1.712 V to reach 1000 mA cm<sup>-2</sup> when assembled in a NiCoPi-NiS/NF || FePi-NiS/NF electrode. Furthermore, such electrodes can reduce energy consumption when coupled with other systems, such as S<sup>2-</sup> degradation, demonstrating their multifunctionality. The scaled-up electrodes (area:  $\approx 25 \text{ cm}^2$ ) also demonstrate outstanding performance in AEMWE, achieving an ultrahigh current of 12.5 A at 1.87 V, with a remarkable energy efficiency of 79.2 % and excellent durability over 30 h under industrial conditions (1 M KOH, 50 °C). This work not only provides insight into the actual active sites of catalysts under industrial current density but also serves as a reference for the rational design of low-cost and highly efficient catalysts for industrial water electrolysis and other electrocatalytic systems.

#### CRedit authorship contribution statement

**Lei Guo:** Experimental Measurements, Writing, Investigation, Formal analysis. **Jing Xie:** Provision of study materials, Data curation. **Shiyi Chen:** Visualization, Data curation. **Zexing He:** Visualization, Data curation, Funding acquisition. **Yuezheng Liu:** Conducting a research and investigation process. **Chengxiang Shi:** Reviewing and Editing, Supervision. **Ruijie Gao:** Reviewing and Editing. **Lun Pan:** Conceptualization, Supervision, Funding acquisition. **Zhen-Feng Huang:** Review and Editing, Supervision, Funding acquisition. **Xiangwen Zhang:** Management and coordination. **Ji-Jun Zou:** Supervision and Funding.

#### Declaration of Competing Interest

The authors declare that they have no known competing financial interests or personal relationships that could have appeared to influence the work reported in this paper.

#### Data availability

Data will be made available on request.

#### Acknowledgements

The authors appreciate the support from the National Key R&D Program of China (2020YFA0710000), the National Natural Science Foundation of China (22278307, 22008170, 22222808, 21978200), the Applied Basic Research Program of Qinghai Province (2023-ZJ-701) and the Tianjin Research Innovation Project for Postgraduate Students (2022BKYZ035).

## Appendix A. Supporting information

Supplementary data associated with this article can be found in the online version at doi:10.1016/j.apcatb.2023.123252.

## References

- [1] J.A. Turner, Sustainable hydrogen production, *Science* 305 (2004) 972–974.
- [2] I. Roger, M.A. Shipman, M.D. Symes, Earth-abundant catalysts for electrochemical and photoelectrochemical water splitting, *Nat. Rev. Chem.* 1 (2017) 0003.
- [3] C. Deng, C.Y. Toe, X. Li, J. Tan, H. Yang, Q. Hu, C. He, Earth-abundant metal-based electrocatalysts promoted anodic reaction in hybrid water electrolysis for efficient hydrogen production: recent progress and perspectives, *Adv. Energy Mater.* 12 (2022), 2201047.
- [4] Z.-F. Huang, J. Song, Y. Du, S. Xi, S. Dou, J.M.V. Nsanzimana, C. Wang, Z.J. Xu, X. Wang, Chemical and structural origin of lattice oxygen oxidation in Co-Zn oxyhydroxide oxygen evolution electrocatalysts, *Nat. Energy* 4 (2019) 329–338.
- [5] M. Batoool, A. Hameed, M.A. Nadeem, Recent developments on iron and nickel-based transition metal nitrides for overall water splitting: a critical review, *Coord. Chem. Rev.* 480 (2023), 215029.
- [6] X. Liu, Y. Yao, H. Zhang, L. Pan, C. Shi, X. Zhang, Z.-F. Huang, J.-J. Zou, In situ grown cobalt-iron phosphide-based integrated electrode for long-term water splitting under a large current density at the industrial electrolysis temperature, *ACS Sustain. Chem. Eng.* 8 (2020) 17828–17838.
- [7] R. Luo, Z. Qian, L. Xing, C. Du, G. Yin, S. Zhao, L. Du, Re-looking into the active moieties of metal X-ides (X=Phosph-, Sulf-, Nitr-, and Carb-) toward oxygen evolution reaction, *Adv. Funct. Mater.* 31 (2021), 2102918.
- [8] X. Zou, Y. Zhang, Noble metal-free hydrogen evolution catalysts for water splitting, *Chem. Soc. Rev.* 44 (2015) 5148–5180.
- [9] H. Ding, H. Liu, W. Chu, C. Wu, Y. Xie, Structural transformation of heterogeneous materials for electrocatalytic oxygen evolution reaction, *Chem. Rev.* 121 (2021) 13174–13212.
- [10] W. He, L. Han, Q. Hao, X. Zheng, Y. Li, J. Zhang, C. Liu, H. Liu, H.L. Xin, Fluorine-anion-modulated electron structure of nickel sulfide nanosheet arrays for alkaline hydrogen evolution, *ACS Energy Lett.* 4 (2019) 2905–2912.
- [11] T. Guo, L. Li, Z. Wang, Recent development and future perspectives of amorphous transition metal-based electrocatalysts for oxygen evolution reaction, *Adv. Energy Mater.* 12 (2022), 2200827.
- [12] Y. Yu, Q. Chen, J. Li, P. Rao, R. Li, Y. Du, C. Jia, W. Huang, J. Luo, P. Deng, Y. Shen, X. Tian, Progress in the development of heteroatom-doped nickel phosphates for electrocatalytic water splitting, *J. Colloid Interface Sci.* 607 (2022) 1091–1102.
- [13] A. Li, X. Chang, Z. Huang, C. Li, Y. Wei, L. Zhang, T. Wang, J. Gong, Thin heterojunctions and spatially separated cocatalysts to simultaneously reduce bulk and surface recombination in photocatalysts, *Angew. Chem. Int. Ed.* 55 (2016) 13734–13738.
- [14] P.W. Menezes, C. Panda, C. Walter, M. Schwarze, M. Driess, A cobalt-based amorphous bifunctional electrocatalysts for water-splitting evolved from a single-source lazulite cobalt phosphate, *Adv. Funct. Mater.* 29 (2019), 1808632.
- [15] C. Zhang, Y. Huang, Y. Yu, J. Zhang, S. Zhuo, B. Zhang, Sub-1.1 nm ultrathin porous CoP nanosheets with dominant reactive {200} facets: a high mass activity and efficient electrocatalyst for the hydrogen evolution reaction, *Chem. Sci.* 8 (2017) 2769–2775.
- [16] Y. Zhang, F. Gao, D. Wang, Z. Li, X. Wang, C. Wang, K. Zhang, Y. Du, Amorphous/crystalline heterostructure transition-metal-based catalysts for high-performance water splitting, *Coord. Chem. Rev.* 475 (2023), 214916.
- [17] B. Zhou, R. Gao, J.-J. Zou, H. Yang, Surface design strategy of catalysts for water electrolysis, *Small* 18 (2022), 2202336.
- [18] S. Shen, Z. Wang, Z. Lin, K. Song, Q. Zhang, F. Meng, L. Gu, W. Zhong, Crystalline-amorphous interfaces coupling of CoSe<sub>2</sub>/CoP with optimized d-band center and boosted electrocatalytic hydrogen evolution, *Adv. Mater.* 34 (2022), 2110631.
- [19] T.I. Singh, A. Maibam, D.C. Cha, S. Yoo, R. Babarao, S.U. Lee, S. Lee, High-alkaline water-splitting activity of mesoporous 3D heterostructures: an amorphous-shell@crystalline-core nano-assembly of Co-Ni-phosphate ultrathin-nanosheets and V-doped cobalt-nitride nanowires, *Adv. Sci.* 9 (2022), 2201311.
- [20] Z. Chen, L. Guo, L. Pan, T. Yan, Z. He, Y. Li, C. Shi, Z.-F. Huang, X. Zhang, J.-J. Zou, Advances in oxygen evolution electrocatalysts for proton exchange membrane water electrolyzers, *Adv. Energy Mater.* 12 (2022), 2103670.
- [21] Y.J. Kim, A. Lim, J.M. Kim, D. Lim, K.H. Chae, E.N. Cho, H.J. Han, K.U. Jeon, M. Kim, G.H. Lee, G.R. Lee, H.S. Ahn, H.S. Park, H. Kim, J.Y. Kim, Y.S. Jung, Highly efficient oxygen evolution reaction via facile bubble transport realized by three-dimensionally stack-printed catalysts, *Nat. Commun.* 11 (2020) 4921.
- [22] H. Sun, Z. Yan, F. Liu, W. Xu, F. Cheng, J. Chen, Self-supported transition-metal-based electrocatalysts for hydrogen and oxygen evolution, *Adv. Mater.* 32 (2020), e1806326.
- [23] H. Yang, M. Driess, P.W. Menezes, Self-supported electrocatalysts for practical water electrolysis, *Adv. Energy Mater.* 11 (2021), 2102074.
- [24] C. Dai, B. Li, J. Li, B. Zhao, R. Wu, H. Ma, X. Duan, Controllable synthesis of NiS and NiS<sub>2</sub> nanoplates by chemical vapor deposition, *Nano Res.* 13 (2020) 2506–2511.
- [25] P.-F. Yin, X.-y Han, C. Zhou, C.-h Xia, C.-l Hu, L.-l Sun, Large-scale synthesis of nickel sulfide micro/nanorods via a hydrothermal process, *Int. J. Miner., Metall., Mater.* 22 (2015) 762–769.
- [26] X. Liu, L. Xu, B. Zhang, Essential elucidation for preparation of supported nickel phosphide upon nickel phosphate precursor, *J. Solid State Chem.* 212 (2014) 13–22.
- [27] X. Bo, R.K. Hocking, S. Zhou, Y. Li, X. Chen, J. Zhuang, Y. Du, C. Zhao, Capturing the active sites of multimetallic (oxy)hydroxides for the oxygen evolution reaction, *Energy Environ. Sci.* 13 (2020) 4225–4237.
- [28] L. Guo, X. Liu, Z. He, Z. Chen, Z. Zhang, L. Pan, Z.-F. Huang, X. Zhang, Y. Fang, J.-J. Zou, Self-supported bimetallic phosphide heterojunction-integrated electrode promoting high-performance alkaline anion-exchange membrane water electrolysis, *ACS Sustain. Chem. Eng.* 10 (2022) 9956–9968.
- [29] D. Zhang, Y. Song, Z. Du, L. Wang, Y. Li, J.B. Goodenough, Active LaNi<sub>1-x</sub>Fe<sub>x</sub>O<sub>3</sub> bifunctional catalysts for air cathodes in alkaline media, *J. Mater. Chem. A* 3 (2015) 9421–9426.
- [30] Q. Wen, K. Yang, D. Huang, G. Cheng, X. Ai, Y. Liu, J. Fang, H. Li, L. Yu, T. Zhai, Schottky heterojunction nanosheet array achieving high-current-density oxygen evolution for industrial water splitting electrolyzers, *Adv. Energy Mater.* 11 (2021), 2102353.
- [31] X. Xu, T. Guo, J. Xia, B. Zhao, G. Su, H. Wang, M. Huang, A. Toghan, Modulation of the crystalline/amorphous interface engineering on Ni-P-O-based catalysts for boosting urea electrolysis at large current densities, *Chem. Eng. J.* 425 (2021), 130514.
- [32] C. Yan, J. Huang, C. Wu, Y. Li, Y. Tan, L. Zhang, Y. Sun, X. Huang, J. Xiong, In-situ formed NiS/Ni coupled interface for efficient oxygen evolution and hydrogen evolution, *J. Mater. Sci. Technol.* 42 (2020) 10–16.
- [33] X. Liu, R. Guo, K. Ni, F. Xia, C. Niu, B. Wen, J. Meng, P. Wu, J. Wu, X. Wu, L. Mai, Reconstruction-determined alkaline water electrolysis at industrial temperatures, *Adv. Mater.* 32 (2020), e2001136.
- [34] Z. Zhang, Y. Zhu, Y. Zhong, W. Zhou, Z. Shao, Anion doping: a new strategy for developing high-performance perovskite-type cathode materials of solid oxide fuel cells, *Adv. Energy Mater.* 7 (2017), 1700242.
- [35] Y. Pan, X. Xu, Y. Zhong, L. Ge, Y. Chen, J.M. Veder, D. Guan, R. O'Hare, M. Li, G. Wang, H. Wang, W. Zhou, Z. Shao, Direct evidence of boosted oxygen evolution over perovskite by enhanced lattice oxygen participation, *Nat. Commun.* 11 (2020) 2002.
- [36] S.Y. Lim, S. Park, S.W. Im, H. Ha, H. Seo, K.T. Nam, Chemically deposited amorphous Zn-doped NiFeO<sub>x</sub>H<sub>y</sub> for enhanced water oxidation, *ACS Catal.* 10 (2019) 235–244.
- [37] L. Yi, Y. Niu, B. Feng, M. Zhao, W. Hu, Simultaneous phase transformation and doping via a unique photochemical–electrochemical strategy to achieve a highly active Fe-doped Ni oxyhydroxide oxygen evolution catalyst, *J. Mater. Chem. A* 9 (2021) 4213–4220.
- [38] L. Lin, R. Xin, M. Yuan, T. Wang, J. Li, Y. Xu, X. Xu, M. Li, Y. Du, J. Wang, S. Wang, F. Jiang, W. Wu, C. Lu, B. Huang, Z. Sun, J. Liu, J. He, G. Sun, Revealing spin magnetic effect of iron-group layered double hydroxides with enhanced oxygen catalysis, *ACS Catal.* 13 (2023) 1431–1440.
- [39] W. Luo, C. Jiang, Y. Li, S.A. Shevlin, X. Han, K. Qiu, Y. Cheng, Z. Guo, W. Huang, J. Tang, Highly crystallized  $\alpha$ -FeOOH for a stable and efficient oxygen evolution reaction, *J. Mater. Chem. A* 5 (2017) 2021–2028.
- [40] T. Wang, X. Li, Y. Pang, X. Gao, Z. Kou, J. Tang, J. Wang, Unlocking the synergy of interface and oxygen vacancy by core-shell nickel phosphide@oxyhydroxide nanosheets arrays for accelerating alkaline oxygen evolution kinetics, *Chem. Eng. J.* 425 (2021), 131491.
- [41] B. Zhang, J. Shan, X. Wang, Y. Hu, Y. Li, Ru/Rh cation doping and oxygen-vacancy engineering of FeOOH nanoarrays@Ti3C2Tx MXene heterojunction for Highly efficient and stable electrocatalytic oxygen evolution, *Small* 18 (2022), 2200173.
- [42] Y. Gan, Y. Ye, X. Dai, X. Yin, Y. Cao, R. Cai, B. Feng, Q. Wang, X. Zhang, La and S co-doping induced the synergism of multiphase nickel-iron nanosheets with rich oxygen vacancies to trigger large-current-density oxygen evolution and urea oxidation reactions, *Small* (2023), 2303250.
- [43] Y. Zhu, W. Zhou, Z.G. Chen, Y. Chen, C. Su, M.O. Tade, Z. Shao, SrNb<sub>0.1</sub>Co<sub>0.7</sub>Fe<sub>0.2</sub>O<sub>3.4</sub> perovskite as a next-generation electrocatalyst for oxygen evolution in alkaline solution, *Angew. Chem. Int. Ed.* 54 (2015) 3897–3901.
- [44] M. Cai, Q. Zhu, X. Wang, Z. Shao, L. Yao, H. Zeng, X. Wu, J. Chen, K. Huang, S. Feng, Formation and stabilization of NiOOH by introducing  $\alpha$ -FeOOH in LDH: Composite electrocatalyst for oxygen evolution and urea oxidation reactions, *Adv. Mater.* 35 (2023), 2209338.
- [45] T. Begildayeva, J. Theerthagiri, S.J. Lee, Y. Yu, M.Y. Choi, Unraveling the synergy of anion modulation on Co electrocatalysts by pulsed laser for water splitting: intermediate capturing by in situ/operando Raman studies, *Small* 18 (2022), e2204309.
- [46] C.V. Ramana, A. Ait-Salah, S. Utsunomiya, U. Becker, A. Mauger, F. Gendron, C. M. Julien, Structural characteristics of lithium nickel phosphate studied using analytical electron microscopy and Raman spectroscopy, *Chem. Mater.* 18 (2006) 3788–3794.
- [47] S.-W Wang, M. Mao, Y. Cao, H.-W Luo, H. Wang, D.-J Guo, Novel cuboid-like cobalt nickel phosphate/manganese dioxide/multi-walled carbon nanotubes composites as binder-free electrodes for high-performance supercapacitors, *Inorg. Chem. Commun.* 114 (2020), 107822.
- [48] X. Yu, Z.-Y. Yu, X.-L. Zhang, P. Li, B. Sun, X. Gao, K. Yan, H. Liu, Y. Duan, M.-R. Gao, G. Wang, S.-H. Yu, Highly disordered cobalt oxide nanostructure induced by sulfur incorporation for efficient overall water splitting, *Nano Energy* 71 (2020), 104652.
- [49] P. Fang, M. Zhu, J. Liu, Z. Zhu, J. Hu, X. Xu, Making ternary-metal hydroxysulfide catalyst via cathodic reconstruction with ion regulation for industrial-level hydrogen generation, *Adv. Energy Mater.* (2023), 2301222.

[50] W. Zhang, Y. Yang, Y. Tang, Q. Gao, In-situ reconstruction of catalysts in cathodic electrocatalysis: new insights into active-site structures and working mechanisms, *J. Energy Chem.* 70 (2022) 414–436.

[51] L. Wang, Y. Hao, L. Deng, F. Hu, S. Zhao, L. Li, S. Peng, Rapid complete reconfiguration induced actual active species for industrial hydrogen evolution reaction, *Nat. Commun.* 13 (2022) 5785.

[52] W. Lai, L. Ge, H. Li, Y. Deng, B. Xu, B. Ouyang, E. Kan, In situ Raman spectroscopic study towards the growth and excellent HER catalysis of Ni/Ni(OH)<sub>2</sub> heterostructure, *Int. J. Hydrog. Energy* 46 (2021) 26861–26872.

[53] A. Mavrić, M. Fanetti, Y. Lin, M. Valant, C. Cui, Spectroelectrochemical tracking of nickel hydroxide reveals its irreversible redox states upon operation at high current density, *ACS Catal.* 10 (2020) 9451–9457.

[54] B. Yang, X. Li, Q. Cheng, X. Jia, Y. Liu, Z. Xiang, A highly efficient axial coordinated CoN<sub>5</sub> electrocatalyst via pyrolysis-free strategy for alkaline polymer electrolyte fuel cells, *Nano Energy* 101 (2022), 107565.

[55] W. He, R. Zhang, D. Cao, Y. Li, J. Zhang, Q. Hao, H. Liu, J. Zhao, H.L. Xin, Super-hydrophilic microporous Ni(OH)<sub>x</sub>/Ni<sub>3</sub>S<sub>2</sub> heterostructure electrocatalyst for large-current-density hydrogen evolution, *Small* 19 (2023), e2205719.

[56] L. Yu, L. Wu, B. McElhenney, S. Song, D. Luo, F. Zhang, Y. Yu, S. Chen, Z. Ren, Ultrafast room-temperature synthesis of porous S-doped Ni/Fe (oxy)hydroxide electrodes for oxygen evolution catalysis in seawater splitting, *Energy Environ. Sci.* 13 (2020) 3439–3446.

[57] X. Kang, F. Yang, Z. Zhang, H. Liu, S. Ge, S. Hu, S. Li, Y. Luo, Q. Yu, Z. Liu, Q. Wang, W. Ren, C. Sun, H.-M. Cheng, B. Liu, A corrosion-resistant RuMoNi catalyst for efficient and long-lasting seawater oxidation and anion exchange membrane electrolyzer, *Nat. Commun.* 14 (2023) 3607.